


Measurement of near-field thermal emission spectra using an internal reflection elementSaman Zare,^{1,*} Carl P. Tripp,^{2,3} and Sheila Edalatpour^{1,3,†}¹*Department of Mechanical Engineering, University of Maine, Orono, Maine 04469, USA*²*Department of Chemistry, University of Maine, Orono, Maine 04469, USA*³*Frontier Institute for Research in Sensor Technologies, University of Maine, Orono, Maine 04469, USA* (Received 6 June 2019; revised manuscript received 19 November 2019; published 26 December 2019)

We describe a simple and robust method using an internal reflection element to measure the spectra of near-field thermal emission. We experimentally demonstrate the spectrally narrow peaks of near-field thermal emission by isotropic media due to the excitation of surface phonon polaritons in quartz and amorphous silica and due to the frustrated total-internal-reflection modes in amorphous silica and polytetrafluoroethylene. Additionally, we demonstrate the broadband near-field thermal emission of hyperbolic modes in hexagonal boron nitride, which is an anisotropic uniaxial medium. We also present a theoretical approach based on the fluctuational electrodynamics and dyadic Green's functions for one-dimensional layered media for accurately modeling the measured spectra.

DOI: [10.1103/PhysRevB.100.235450](https://doi.org/10.1103/PhysRevB.100.235450)**I. INTRODUCTION**

Many near-field applications, such as nanogap thermophotovoltaic power generation [1–8] and thermal rectification [9–21], rely on spectrally selective thermal emission in the near field. Most of the experimental studies on near-field thermal radiation have measured the total (spectrally integrated) heat transfer which does not provide information about the spectrum of heat transfer [7,22–49]. Narrow peaks can be observed in the near-field thermal emission by isotropic media due to the excitation of surface phonon and plasmon polaritons (SPhPs and SPPs, respectively) as well as frustrated total-internal-reflection modes. In addition to surface and frustrated modes, anisotropic media can support hyperbolic modes that enhance near-field thermal emission in a broadband manner. Measuring the spectrum of near-field thermal emission is challenging because the evanescent waves in the near-field need to be converted to propagating waves to reach a Fourier-transform infrared (FTIR) spectrometer located in the far zone. So far, the SPhP modes of near-field thermal emission have been measured for silica [50,51], quartz [52], silicon carbide (SiC) [50,52–54], and for a thin film of hexagonal boron nitride (hBN) on gold and silica substrates [54]. The frustrated total-internal-reflection modes thermally emitted by polytetrafluoroethylene (PTFE) have also been measured [52,54]. However, the broadband near-field thermal emission due to hyperbolic modes has not been experimentally observed.

Most of the measured near-field spectra are obtained using scanning optical microscopes [50,52–54]. In this spectroscopic technique, the thermal near field of an emitting sample is scattered to the far zone by bringing the sharp tip of the microscope to a sub-wavelength distance from the sample. The measured peaks using this technique are redshifted (from

3 to 63 cm⁻¹) and broadened relative to the theoretical predictions using the fluctuational electrodynamics [50–56]. It is shown experimentally [53], and theoretically [56], that the spectral redshift and broadening of the peaks are strongly dependent on the geometry of the probe. For example, three different values of 898, 923, and 943 cm⁻¹ were obtained for the SPhP resonance of SiC when different probes were used in the same experimental setup [53]. The reason for the three different values for the resonance arises from the difficulty in precisely controlling and measuring the geometry of the probe. Furthermore, computationally expensive numerical models are required for relating the measured signal to the near-field thermal emission by the sample.

In this study, we present a simple and robust spectroscopy technique which does not involve multiscale, complex-shape probes and specialized optical instruments. In addition to SPhP and frustrated modes for quartz, silica and PTFE, we experimentally demonstrate broadband hyperbolic thermal emission for hBN. The measured spectra are reproducible, and the redshift and broadening of the peaks can accurately be predicted using a theoretical model based on the fluctuational electrodynamics and dyadic Green's functions (DGFs) for one-dimensional layered media.

II. EXPERIMENTAL SETUP

A schematic of the experimental setup for near-field thermal emission spectroscopy is shown in Fig. 1(a). An internal reflection element (IRE) which has low infrared losses is brought into contact with an emitting sample. Due to surface roughness, several sub-wavelength air gaps are formed between the two surfaces. The air gap due to surface roughness is represented by d in Fig. 1(b) where a close-up view of the sample-IRE interface is shown. The emitted evanescent waves with parallel component of the wave vector, k_{ρ} , between k_0 and $n_I k_0$ (k_0 and n_I are vacuum wave vector and IRE refractive index, respectively) are converted into

*saman.zare@maine.edu

†sheila.edalatpour@maine.edu

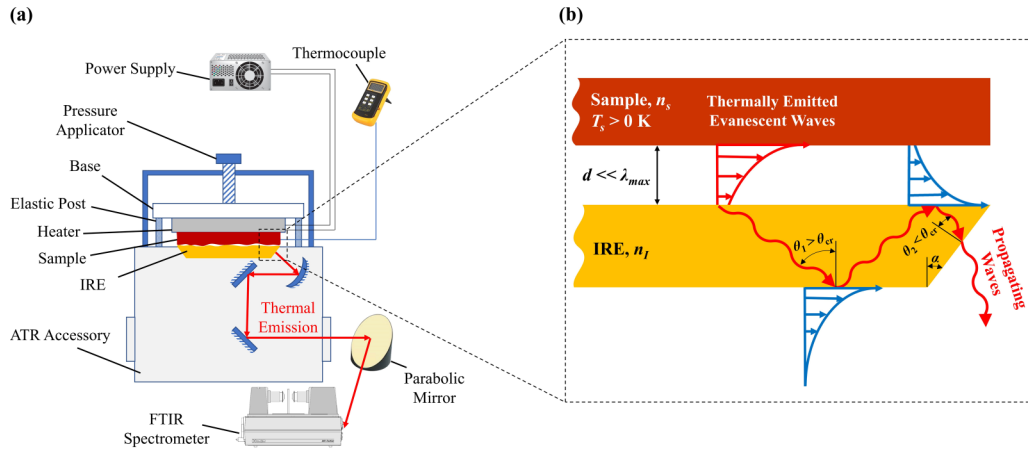


FIG. 1. (a) A schematic of the experimental setup for near-field thermal emission spectroscopy. (b) A close-up view of the sample-IRE interface. The distance d represents the air gap between the sample and the IRE due to surface roughness. Thermally emitted evanescent waves with k_p between k_0 and $\sin(90^\circ - \alpha + \theta_{cr})n_I k_0$ exit the IRE's beveled ends after several total internal reflections, and are collected using an FTIR spectrometer.

propagating waves in the IRE due to the increase of the wave vector [Fig. 1(b)]. These propagating waves cannot escape the parallel surfaces of the IRE as they experience total internal reflections. Instead, these modes travel through the IRE toward its beveled ends which make an angle of α with the surface normal. The coupled modes with k_p between k_0 and $\sin(90^\circ - \alpha + \theta_{cr})n_I k_0$, where $\theta_{cr} = \sin^{-1}(1/n_I)$ is the critical angle for the IRE-air interface, hit the IRE beveled ends with an angle smaller than the critical angle (see Sec. I of the Supplemental Material [57]). These modes exit from IRE's beveled ends and are sent to an FTIR spectrometer where their spectrum is recorded. The higher the refractive index and the bevel angle of the IRE, the larger the number of evanescent modes that can couple to the IRE. Since the IRE is transparent in the infrared, its thermal emission is negligible compared to the sample. The arrangement shown in Fig. 1(b) is similar to the inverse of the Kretschmann configuration used for exciting SPPs at the interface of a metallic thin film and the free space using an external illumination [58].

The sample is mounted on a metal ceramic heater with an output of 24 W at 24 V (Thorlabs, HT24S), which is connected to a power supply (KEPCO, ABC 36-3DM) with a maximum voltage of 36 V. The sample temperature is measured using a K -type thermocouple and is read using a digital thermometer (OMEGA, HH-52). The sample-heater assembly is adhered to a ceramic base using a nickel-base metallic adhesive (Cotronics Corp., Durabond 952 FS). A zinc selenide (ZnSe) IRE with a trapezoidal cross section and a bevel angle of $\alpha = 45^\circ$ is selected for the experiment (Harrick, EM2122). The IRE dimensions are 50 (length) \times 10 (width) \times 2 (thickness) mm. ZnSe has a refractive index of $n_I \approx 2.4$ and is transparent between 700 and 15000 cm^{-1} . The IRE is placed on the sampling surface of a multiple-reflection horizontal Attenuated Total Reflection (ATR) accessory (Harrick, HorizonTM). The base-heater-sample assembly is put in contact with the IRE while two elastic posts made of 0.005"-thick stainless-steel plates acting as a spring are placed between the base and the sampling plate of the ATR accessory.

A pressure applicator is used to press the base toward the IRE for near-field measurements. For far-field measurements, the pressure is released from the base such that the elastic posts push the sample away and keep it at a 1-mm distance from the IRE. The signal exiting one of the IRE beveled ends is collected by the ATR accessory and transferred into the emission port of an FTIR spectrometer using an $f/4$ parabolic mirror. The FTIR is an ABB-Bomem MB1552E equipped with a broadband mercury-cadmium-telluride detector (Infrared Associates Inc.).

III. RESULTS AND DISCUSSION

Near-field and far-field thermal spectra are measured for quartz, silica, PTFE, and hBN at a temperature of approximately 160 $^\circ\text{C}$ (see Sec. II of the Supplemental Material [57]). The silica, hBN, and PTFE samples are 1-mm thick, while the thicknesses of the quartz sample is 0.5 mm. It is verified experimentally and theoretically that all samples are optically thick. A spectral resolution of 4 cm^{-1} is selected for the FTIR spectrometer. The background thermal emission is measured by blocking the sample emission from reaching the FTIR via placing a thick film of stainless steel (which is opaque in the infrared) at the exit of the ATR accessory. The background thermal emission is subtracted from the measured signals. The near-field spectra are normalized by the far-field thermal emission to compensate for the wave-number-dependent responsivity of the photodetector, absorption by the internal parts of the ATR accessory and ambient gases, as well as modulation efficiency of the FTIR spectrometer (see Sec. III of the Supplemental Material [57]). The normalized near-field spectra are shown in Figs. 2(a)–2(d). To ensure that the experiments are reproducible, the measurements were repeated three times for each sample. In each repetition, the IRE, the sample, and the heater are disassembled and reinstalled. As an example, the three measured spectra for the quartz sample are plotted in Fig. 2(a). This level of repeatability was observed for all samples.

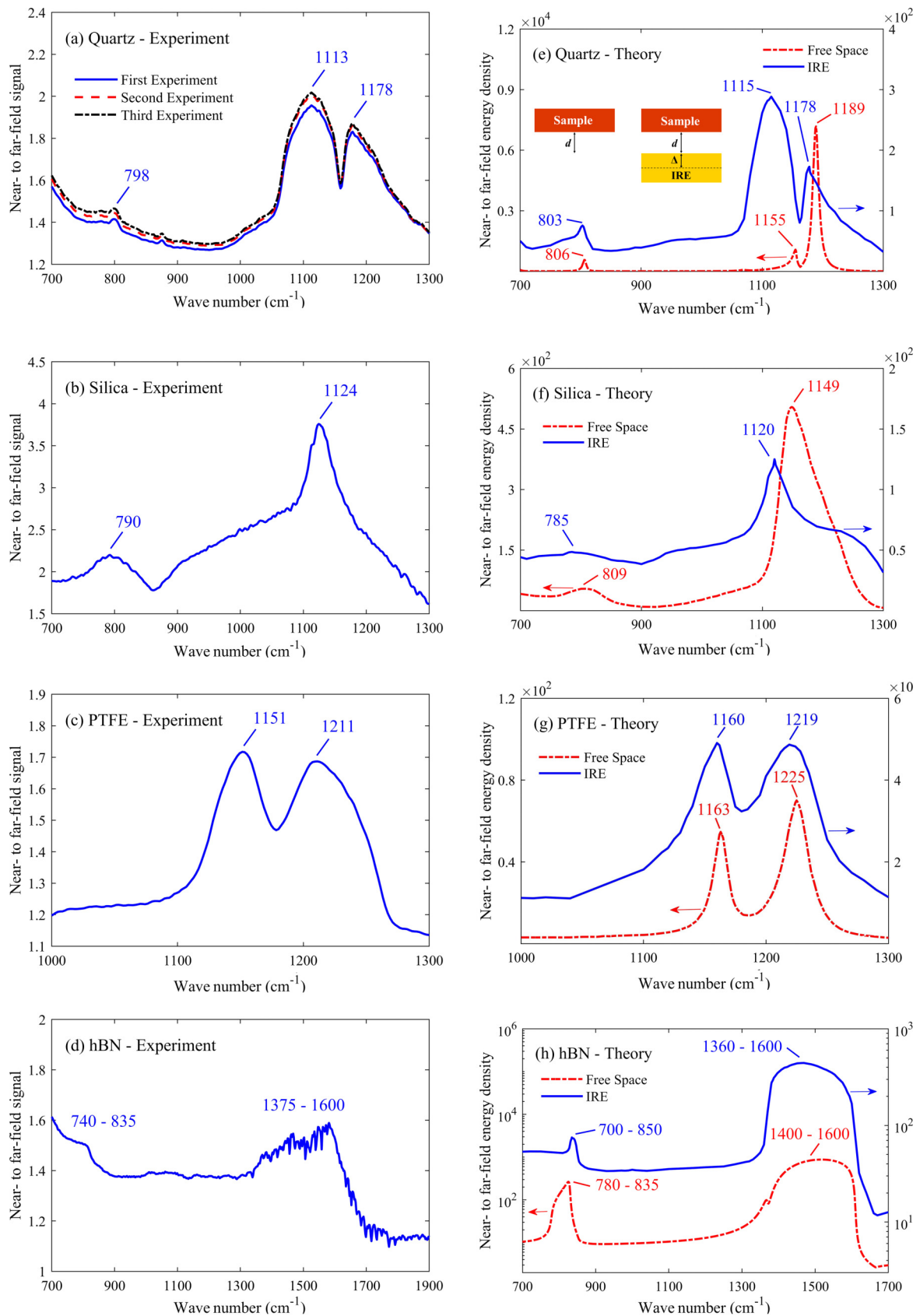


FIG. 2. The near-field thermal emission spectra normalized by the far-field value for quartz, silica, PTFE, and hBN. Panels (a)–(d) show the measured spectra, while Panels (e)–(h) display theoretically predicted spectra. In Panels (e)–(h), red dashed lines show the energy density at distance d in the free space, while the solid blue lines show the energy density at distance Δ in the IRE due to the modes with k_x between $\sin(20.4^\circ)n_l k_0$ and $\sin(69.6^\circ)n_l k_0$.

To compare measurements with theory, the energy density emitted by the samples in free space (integrated over k_ρ from 0 to infinity) is calculated using the fluctuational electrodynamics and the DGFs for a semi-infinite bulk [59–62]. The near-field and far-field energy densities are calculated at 200 nm (approximately equal to the surface flatness of the samples) and 1 mm above the samples, respectively. The dielectric functions of quartz, silica, PTFE, and hBN are obtained from literature [63–65] and are plotted in Sec. IV of the Supplemental Material [57]. It should be noted that hBN is an anisotropic uniaxial medium and is described using a parallel and a perpendicular (to the optical axis) dielectric function. The calculated near-field spectra normalized by their far-field value are plotted in Figs. 2(e)–2(h). Peaks in near-field thermal spectra occur when $\varepsilon_s + 1 \rightarrow 0$ (due to the excitation of SPhPs) and $\text{Im}[\varepsilon_s] \rightarrow \infty$ (due to the contribution of frustrated total-internal-reflection modes), where $\varepsilon_s = n_s^2$ is the dielectric function of the sample [66]. Additionally, thermal emission by uniaxial media can be enhanced in a broadband manner when $\text{Re}[\varepsilon_{s,\parallel}]\text{Re}[\varepsilon_{s,\perp}] < 0$ ($\varepsilon_{s,\parallel}$ and $\varepsilon_{s,\perp}$ are the dielectric functions of the sample in the parallel and perpendicular directions relative to the optical axis, respectively) due to the excitation of hyperbolic modes.

The near-field energy density for quartz [Fig. 2(e)] has three peaks at 806, 1155, and 1189 cm^{-1} due to the excitation of surface phonon polaritons ($\text{Re}[\varepsilon_s] = -0.5, -1.4,$ and -1.0 , respectively). The three SPhP resonances are captured in the measured quartz spectrum [Fig. 2(a)]. The SPhP resonances are redshifted and broadened in the experiments compared to the theoretical predictions. The origin of the redshift and broadening of the peaks will be discussed later using a theoretical model. The theoretical energy density for silica [Fig. 2(f)] shows two peaks at 809 and 1149 cm^{-1} which both are measured [Fig. 2(b)]. The low-wave-number peak

is due to the symmetric Si-O-Si stretching vibrations (frustrated modes), while the high-wave-number peak is because of the excitation of SPhPs ($\text{Re}[\varepsilon_s] = -1.2$). The theoretical spectrum for PTFE [Fig. 2(g)] has two peaks at 1163 and 1225 cm^{-1} , which are due to the symmetric and asymmetric C-F stretching vibrations (frustrated modes). These peaks are also captured in the measured spectrum [Fig. 2(c)]. The experimental and theoretical spectra of near-field thermal emission by hBN are shown in Figs. 2(d) and 2(h), respectively. Hexagonal boron nitride has two hyperbolic bands at 780–835 cm^{-1} and 1400–1600 cm^{-1} . These two hyperbolic bands are captured in the measured spectrum of hBN in Fig. 2(d). The increase of the measured signal near 700 cm^{-1} is due to thermal emission by ZnSe which becomes opaque around this wave number.

The measured near-field peaks are broadened and exhibit redshifts ranging from 8 to 42 cm^{-1} . Peak broadening and redshifts up to 105 cm^{-1} are also observed in previously measured spectra [50–56]. The redshift and broadening in our measurements can be predicted by modeling energy density in the IRE due to thermal emission by the sample. The energy density at distance Δ in the IRE due to thermal emission by an anisotropic uniaxial medium separated by an air gap of size d from the IRE [see the inset of Fig. 2(e)] is derived in Sec. V of the Supplemental Material [57]. The energy density in the IRE is derived using the fluctuational electrodynamics and the DGFs for a one-dimensional layered media. We have verified that an air gap exists between the sample and the IRE, and that the gap can be adjusted by depositing polystyrene nanoparticles on the IRE (see Secs. VI and VII of the Supplemental Material [57]). The energy density of the modes exiting the IRE beveled ends, i.e., modes with k_ρ between $\sin(20.4^\circ)n_l k_0$ and $\sin(69.6^\circ)n_l k_0$ (see Sec. I of the Supplemental Material [57]), is derived as

$$\langle u(\Delta, \omega) \rangle = \frac{\Theta(\omega, T_s)\omega}{2c_0^2\pi^2} \int_{\sin(20.4^\circ)n_l k_0}^{\sin(69.6^\circ)n_l k_0} k_\rho \int_0^{t_s} (k_l^2 \text{Trace}[\bar{\mathbf{g}}^E(k_\rho, \Delta, z', \omega)] \text{Im}[\bar{\varepsilon}_s] \bar{\mathbf{g}}^{E\dagger}(k_\rho, \Delta, z', \omega)) + \text{Trace}[\bar{\mathbf{g}}^H(k_\rho, \Delta, z', \omega)] \text{Im}[\bar{\varepsilon}_s] \bar{\mathbf{g}}^{H\dagger}(k_\rho, \Delta, z', \omega)) dz' dk_\rho. \quad (1)$$

In Eq. (1), u is the energy density, ω is the angular frequency, Θ is the mean energy of an electromagnetic state [60], $\langle \rangle$ represents ensemble average, c_0 is the speed of light in the free space, T_s is the sample temperature, t_s is the thickness of the sample, k_l is the wave vector in the IRE, z' is the vertical (to the surface) position of a thermally emitting source in the sample, the superscript \dagger indicates the Hermitian operator, $\bar{\varepsilon}_s (= \text{diag}[\varepsilon_{s,\perp}; \varepsilon_{s,\perp}; \varepsilon_{s,\parallel}])$ is the dielectric-function tensor for the sample, and $\bar{\mathbf{g}}^E$ and $\bar{\mathbf{g}}^H$ are the Weyl components of the electric (E) and magnetic (H) DGFs for an emitting anisotropic medium, respectively. The Weyl components of the DGFs are derived using the scattering matrix method [67] in Sec. V of the Supplemental Material [57].

The energy density in the middle of the IRE (where the signal is collected using the ATR accessory)

is calculated in the near and far fields for a sample temperature of 160 °C. The ratio of the near-field and far-field energy densities is shown in Figs. 2(e)–2(h) for the four samples. The calculated spectra are in great agreement with the measurements showing that Eq. (1) can be used for predicting the redshift and broadening of the near-field peaks. These redshifts and broadening arise from the multiple reflections of the thermally emitted waves between the sample and the IRE as well as the fact that a portion of the near-field evanescent waves are captured in the measurements. However, all the SPhP, frustrated, and hyperbolic modes are captured in the measured spectra. The number of captured modes can be increased by using an IRE with a higher refractive index or using a hemispherical IRE (see Sec. I of the Supplemental Material [57]).

IV. CONCLUSIONS

In summary, we experimentally demonstrated narrow peaks of near-field thermal emission due to the excitation of SPhPs (for quartz and silica) and frustrated total-internal-reflection modes (for silica and PTFE), as well as the broadband thermal emission of hyperbolic modes in the near field (for hBN). We derived an analytical expression for the en-

ergy density inside the IRE due to thermal emission by an anisotropic medium that can be used for predicting the redshift and broadening of the measured near-field peaks.

ACKNOWLEDGMENT

The authors acknowledge support from the National Science Foundation under Grant No. CBET-1804360.

-
- [1] R. S. DiMatteo, P. Greiff, S. L. Finberg, K. A. Young-Waithe, H. K. H. Choy, M. M. Masaki, and C. G. Fonstad, *Appl. Phys. Lett.* **79**, 1894 (2001).
- [2] M. D. Whale and E. G. Cravalho, *IEEE Trans. Energy Convers.* **17**, 130 (2002).
- [3] M. Laroche, R. Carminati, and J.-J. Greffet, *J. Appl. Phys.* **100**, 063704 (2006).
- [4] K. Park, S. Basu, W. P. King, and Z. M. Zhang, *J. Quant. Spectrosc. Radiat. Transf.* **109**, 305 (2008).
- [5] M. Francoeur, R. Vaillon, and M. P. Mengüç, *IEEE Trans. Energy Convers.* **26**, 686 (2011).
- [6] M. P. Bernardi, O. Dupré, E. Blandre, P.-O. Chapuis, R. Vaillon, and M. Francoeur, *Sci. Rep.* **5**, 11626 (2015).
- [7] A. Fiorino, L. Zhu, D. Thompson, R. Mittapally, P. Reddy, and E. Meyhofer, *Nat. Nanotechnol.* **13**, 806 (2018).
- [8] E. Tervo, E. Bagherisereshki, and Z. Zhang, *Front. Energy* **12**, 5 (2018).
- [9] C. R. Otey, W. T. Lau, and S. Fan, *Phys. Rev. Lett.* **104**, 154301 (2010).
- [10] S. Basu and M. Francoeur, *Appl. Phys. Lett.* **98**, 113106 (2011).
- [11] P. J. van Zwol, K. Joulain, P. Ben Abdallah, J. J. Greffet, and J. Chevrier, *Phys. Rev. B* **83**, 201404(R) (2011).
- [12] H. Iizuka and S. Fan, *J. Appl. Phys.* **112**, 024304 (2012).
- [13] Y. Yang, S. Basu, and L. Wang, *Appl. Phys. Lett.* **103**, 163101 (2013).
- [14] L. P. Wang and Z. M. Zhang, *Nanosc. Microsc. Thermophys. Eng.* **17**, 337 (2013).
- [15] K. Ito, K. Nishikawa, H. Iizuka, and H. Toshiyoshi, *Appl. Phys. Lett.* **105**, 253503 (2014).
- [16] K. Joulain, Y. Ezzahri, J. Drevillon, B. Rousseau, and D. D. S. Meneses, *Opt. Express* **23**, A1388 (2015).
- [17] A. Ghanekar, J. Ji, and Y. Zheng, *Appl. Phys. Lett.* **109**, 123106 (2016).
- [18] Z. Zheng, X. Liu, A. Wang, and Y. Xuan, *Int. J. Heat Mass Transf.* **109**, 63 (2017).
- [19] K. Ito, K. Nishikawa, A. Miura, H. Toshiyoshi, and H. Iizuka, *Nano Lett.* **17**, 4347 (2017).
- [20] M. Elzouka and S. Ndao, *Sci. Rep.* **7**, 44901 (2018).
- [21] A. Fiorino, D. Thompson, L. Zhu, R. Mittapally, S.-A. Biehs, O. Bezenecenet, N. El-Bondry, S. Bansropun, P. Ben-Abdallah, and E. Meyhofer, *ACS Nano* **12**, 5774 (2018).
- [22] A. Kittel, W. Müller-Hirsch, J. Parisi, S.-A. Biehs, D. Reddig, and M. Holthaus, *Phys. Rev. Lett.* **95**, 224301 (2005).
- [23] L. Hu, A. Narayanaswamy, X. Chen, and G. Chen, *Appl. Phys. Lett.* **92**, 133106 (2008).
- [24] U. F. Wischnath, J. Welker, M. Munzel, and A. Kittel, *Rev. Sci. Instrum.* **79**, 073708 (2008).
- [25] A. Kittel, U. F. Wischnath, J. Welker, O. Huth, F. Rueting, and S.-A. Biehs, *Appl. Phys. Lett.* **93**, 193109 (2008).
- [26] S. Shen, A. Narayanaswamy, and G. Chen, *Nano Lett.* **9**, 2909 (2009).
- [27] E. Rousseau, A. Siria, G. Jourdan, S. Volz, F. Comin, J. Chevrier, and J.-J. Greffet, *Nat. Photonics* **3**, 514 (2009).
- [28] R. S. Ottens, V. Quetschke, S. Wise, A. A. Alemi, R. Lundock, G. Mueller, D. H. Reitze, D. B. Tanner, and B. F. Whiting, *Phys. Rev. Lett.* **107**, 014301 (2011).
- [29] S. Shen, A. Mavrokefalos, P. Sambegoro, and G. Chen, *Appl. Phys. Lett.* **100**, 233114 (2012).
- [30] T. Kralik, P. Hanzelka, M. Zobac, V. Musilova, T. Fort, and M. Horak, *Phys. Rev. Lett.* **109**, 224302 (2012).
- [31] J. Shi, P. Li, B. Liu, and S. Shen, *Appl. Phys. Lett.* **102**, 183114 (2013).
- [32] L. Worbes, D. Hellmann, and A. Kittel, *Phys. Rev. Lett.* **110**, 134302 (2013).
- [33] B. Song, Y. Ganjeh, S. Sadat, D. Thompson, A. Fiorino, V. Fernández-Hurtado, J. Feist, F. J. García-Vidal, J. C. Cuevas, and P. Reddy, *Nat. Nanotechnol.* **10**, 253 (2015).
- [34] T. Ijiri and N. Yamada, *Appl. Phys. Lett.* **106**, 023103 (2015).
- [35] M. Lim, S. S. Lee, and B. J. Lee, *Phys. Rev. B* **91**, 195136 (2015).
- [36] K. Kim, B. Song, V. Fernández-Hurtado, W. Lee, W. Jeong, L. Cui, D. Thompson, J. Feist, M. T. H. Reid, and F. J. García-Vidal, *Nature (London)* **528**, 387 (2015).
- [37] S. A. Dyakov, J. Dai, M. Yan, and M. Qiu, *J. Phys. D* **48**, 305104 (2015).
- [38] B. Song, D. Thompson, A. Fiorino, Y. Ganjeh, P. Reddy, and E. Meyhofer, *Nat. Nanotechnol.* **11**, 509 (2016).
- [39] R. St-Gelais, L. Zhu, S. Fan, and M. Lipson, *Nat. Nanotechnol.* **11**, 515 (2016).
- [40] M. P. Bernardi, D. Milovich, and M. Francoeur, *Nat. Commun.* **7**, 12900 (2016).
- [41] J. I. Watjen, B. Zhao, and Z. M. Zhang, *Appl. Phys. Lett.* **109**, 203112 (2016).
- [42] S. Lang, G. Sharma, S. Molesky, P. U. Kränzien, T. Jalas, Z. Jacob, A. Y. Petrov, and M. Eich, *Sci. Rep.* **7**, 13916 (2017).
- [43] K. Kloppstech, N. Könné, S.-A. Biehs, A. W. Rodriguez, L. Worbes, D. Hellmann, and A. Kittel, *Nat. Commun.* **8**, 14475 (2017).
- [44] L. Cui, W. Jeong, V. Fernández-Hurtado, J. Feist, F. J. García-Vidal, J. C. Cuevas, E. Meyhofer, and P. Reddy, *Nat. Commun.* **8**, 14479 (2017).
- [45] F. Peragut, L. Cerruti, A. Baranov, J. P. Hugonin, T. Taliercio, Y. De Wilde, and J. J. Greffet, *Optica* **4**, 1409 (2017).

- [46] D. Thompson, L. Zhu, R. Mittapally, S. Sadat, Z. Xing, P. McArdle, M. M. Qazilbash, P. Reddy, and E. Meyhofer, *Nature (London)* **561**, 216 (2018).
- [47] M. Ghashami, H. Geng, T. Kim, N. Iacopino, S. K. Cho, and K. Park, *Phys. Rev. Lett.* **120**, 175901 (2018).
- [48] J. Yang, W. Du, Y. Su, Y. Fu, S. Gong, S. He, and Y. Ma, *Nat. Commun.* **9**, 4033 (2018).
- [49] A. Jarzembki, C. Shaskey, and K. Park, *Front. Energy* **12**, 43 (2018).
- [50] A. Babuty, K. Joulain, P.-O. Chapuis, J.-J. Greffet, and Y. De Wilde, *Phys. Rev. Lett.* **110**, 146103 (2013).
- [51] J. K.-K. Tong, *Photonic Engineering of Near-and Far-Field Radiative Heat Transfer* (MIT, Cambridge, MA, 2016).
- [52] A. C. Jones and M. B. Raschke, *Nano Lett.* **12**, 1475 (2012).
- [53] B. T. O'Callahan, W. E. Lewis, A. C. Jones, and M. B. Raschke, *Phys. Rev. B* **89**, 245446 (2014).
- [54] B. T. O'Callahan and M. B. Raschke, *APL Photonics* **2**, 021301 (2017).
- [55] V. Hatamipour, S. Edalatpour, and M. Francoeur, *Phys. Rev. Appl.* **10**, 54047 (2018).
- [56] S. Edalatpour, V. Hatamipour, and M. Francoeur, *Phys. Rev. B* **99**, 165401 (2019).
- [57] See Supplemental Material at <http://link.aps.org/supplemental/10.1103/PhysRevB.100.235450> for determining the modes exciting the IRE; measuring the temperature of the sample; subtracting background thermal emission; dielectric functions of the samples; deriving energy density inside the IRE; and verifying and adjusting the air gap between the sample and the IRE.
- [58] S. A. Maier, *Plasmonics: Fundamentals and Applications* (Springer Science, Berlin, 2007).
- [59] S. M. Rytov, Y. A. Kravtsov, and V. Tatarskii, *Principles of Statistical Radiophysics 3: Elements of Random Fields* (Springer, New York, 1989).
- [60] K. Joulain, J.-P. Mulet, F. Marquier, R. Carminati, and J.-J. Greffet, *Surf. Sci. Rep.* **57**, 59 (2005).
- [61] Y. Guo and Z. Jacob, *J. Appl. Phys.* **115**, 234306 (2014).
- [62] S. Lang, M. Tschikin, S. A. Biehs, A. Y. Petrov, and M. Eich, *Appl. Phys. Lett.* **104**, 121903 (2014).
- [63] E. D. Palik, *Handbook of Optical Constants of Solids* (Academic, New York, 1997).
- [64] E. H. Korte and A. Röseler, *Anal. Bioanal. Chem.* **382**, 1987 (2005).
- [65] Y. Cai, L. Zhang, Q. Zeng, L. Cheng, and Y. Xu, *Solid State Commun.* **141**, 262 (2007).
- [66] J.-P. Mulet, K. Joulain, R. Carminati, and J.-J. Greffet, *Microsc. Thermophys. Eng.* **6**, 209 (2002).
- [67] M. Francoeur, M. P. Mengüç, and R. Vaillon, *J. Quant. Spectrosc. Radiat. Transf.* **110**, 2002 (2009).